

Article

Gemology, Mineralogy, and Spectroscopy of Gem-Quality Diopside from Pakistan and Russia: New Insights for the Chromogenic Mechanism and Possible Origin

Zixuan Wang ^{1,*}, Xiaoqing He ^{2,*}, Bo Xu ^{1,3,4} and Jing Ren ¹

¹ School of Gemology, China University of Geosciences Beijing, 29 Xueyuan Road, Haidian District, Beijing 100083, China; xubo@outlook.com.cn (B.X.)

² Zhongjin Gold Co., Ltd., Beijing 100011, China

³ State Key Laboratory of Geological Processes and Mineral Resources, China University of Geosciences, Beijing 100083, China

⁴ The Beijing SHRIMP Center, Chinese Academy of Geological Sciences, Beijing 100037, China

* Correspondence: wangzx@cugb.edu.cn (Z.W.); hexiaoqing1973@163.com (X.H.)

Abstract: Green diopside is currently popular in the jewelry market due to its attractive color and excellent transparency. Gem-quality diopsides are mainly sourced from Pakistan, Italy, Russia, and other places. The color, geographic origin, and formation mechanism are the main factors affecting the value of gemstones, which can be determined by examining their gemology and composition characteristics. This study systematically characterizes the standard gemology of green diopsides from Pakistan and Russia and compares them with the blue diopsides produced within the skarn process and the diopsides from the nearby region in Russia from previous studies by gemological microscopy, spectral testing (infrared, Raman and ultraviolet-visible spectroscopy), and chemical analyses (electron probe and laser ablation inductively coupled plasma mass spectrometry). The results show that the spectral characteristics and phase composition of the green diopside samples from Pakistan and Russia have excellent uniformity and similarity. The high Cr, Fe, V, and Ni contents are the reasons why they appear as green. Meanwhile, the elemental characteristics of the diopside are effective tools for distinguishing different origins of different diopsides. The Russian green diopsides have higher contents of Sr, Sc, Zr, and rare earth elements (REE), indicating that they are related to alkaline ultrabasic rocks, and the source of the diopside sample from Pakistan is metamorphic rock.

Keywords: diopside; gemological characteristics; LA-ICP-MS; chromogenic mechanism



Citation: Wang, Z.; He, X.; Xu, B.; Ren, J. Gemology, Mineralogy, and Spectroscopy of Gem-Quality Diopside from Pakistan and Russia: New Insights for the Chromogenic Mechanism and Possible Origin. *Crystals* **2023**, *13*, 727. <https://doi.org/10.3390/cryst13050727>

Academic Editor: Vladislav V. Gurzhiy

Received: 2 April 2023
Revised: 13 April 2023
Accepted: 18 April 2023
Published: 25 April 2023



Copyright: © 2023 by the authors. Licensee MDPI, Basel, Switzerland. This article is an open access article distributed under the terms and conditions of the Creative Commons Attribution (CC BY) license (<https://creativecommons.org/licenses/by/4.0/>).

1. Introduction

Diopside is commonly found in metamorphic and igneous rocks, and gem-quality varieties are mainly exploited in Myanmar, Canada, China, Pakistan, Italy, South Africa, Russia, the United States, Austria, India, and other places (Figure 1). Diopside is a mineral with a structure of silicate tetrahedra, linked by sharing oxygen as a single chain, belonging to the pyroxene group, with an ideal formula of $\text{CaMg}[\text{Si}_2\text{O}_6]$. The general formula of pyroxenes is $\text{M}_2\text{M}_1\text{T}_2\text{O}_6$, where M2 structural position is occupied by the cations coordinated by 6–8 oxygen atoms in the generally distorted octahedral coordination. An M1 structural position is occupied by cations with six-fold coordination in the regular octahedral coordination, with Si^{4+} occupying the tetrahedral position T. Si^{4+} occupying the T-site can be replaced by Al^{3+} and Fe^{3+} in the case of the silica undersaturated end members of the group. The M1 site is occupied by Mg^{2+} , Fe^{2+} , Co^{2+} , Fe^{3+} , Cr^{3+} , etc., while the Ca^{2+} mainly occupying the M2 site can be replaced by Na^+ , Mg^{2+} , and Fe^{2+} . Single chains of SiO_4 tetrahedra extending parallel to the *c* axis determine the monoclinic crystal structure of pyroxene in the space group $\text{C}2/c$. The chain structure offers much flexibility in the incorporation of various cations, which is limited by the size of the sites in the structure and the charge of the substituting ions [1–11].



Figure 1. Statistical diagram of the global gem-diopside origins. The gray shaded areas are the countries of gem-diopside origins. The red dots are the locations of the diopside samples from Pakistan and Russia.

Due to the increasing demand in the jewelry market and the discovery of many jewelry deposits producing diopside worldwide, the appeal of diopside has increased considerably. In the literature, there are far more studies on gem-quality diopside from Russia and Italy than those from other regions. Meanwhile, the present studies of gem-quality diopside are almost limited to gemological basic tests, lacking systematic studies of spectral and compositional characteristics, as well as systematic comparisons of diopsides output from different regions [11–14].

In this paper, gem-quality diopsides from Pakistan and Russia were selected (Figure 1), and gemological, spectroscopic, and major and trace element analyses were conducted to determine the gemological and compositional characteristics of these crystals. Meanwhile, we also collected the data of gem-quality blue diopsides from Italy and more Russian diopsides from previous studies, aiming to explore the mechanism of coloration and genetic differences of different diopsides [15,16]. This study can enrich the theoretical, gemological, and mineralogical knowledge of diopside and provide a better understanding of the geological background producing these different diopsides.

2. Geological Setting

The Shigar valley, located about 32 km north of Skardu, is one of the most famous valleys of the Gilgit-Baltistan region of Pakistan, as it is the gateway for most of the expeditions to the K-2, the second highest peak of the world. This valley comprises the Himalayan collision zone, illustrated by the Karakoram mountain ranges (KMR) and the Kohistan-Ladakh Island Arc (KLIA), which possessed a complex history of crustal evolution. The KMR exposed in the Shigar Valley comprises predominantly granitoids, amphibolite, locally granulite-grade polyphase deformed sedimentary rocks, and orthogneiss [17–20]. A large number of pegmatites are also produced in the Shigar valley. Diopside has been reported mainly in the pegmatites and also in the metamorphic rocks of the Shigar valley [18,21–27]. The diopside sample from Pakistan in this study was obtained from skarn formed by metamorphism of limestone.

The Inagli deposit is located within the Inagli massif of alkaline ultramafic rocks of the potassic series, 30 km west of the city of Aldan, Yakutia, Russia [12,28]. The massif is topographically manifested as a cupola structure with a central caldera. The central part of the massif is made up of forsterite dunites, surrounded by alkali gabbroids and pulaskites. The gabbroids are mainly shonkinites grading into mica-bearing pyroxenites, and the pulaskites are accompanied by alkaline pegmatites. Sheet intrusions of syenite porphyry

occur at the periphery of the massif within the Cambrian carbonate sequence. The major units of the geologic structure of the deposit are the country dunites, hosting numerous pegmatite veins composed of early diopside-bearing and late amphibole–feldspar varieties. The deposit contains ten chrome diopside-bearing vein zones, among which only one is of economic importance [12,29–32]. Alkaline pegmatite veins of dunite and the feldspar–diopside metasomatic rocks are the primary sources of diopside in this region [12–14,29,33].

3. Materials and Methods

3.1. Samples Description

Standard gemological tests were performed on two diopside samples (PKD and RUS) from Pakistan and Russia, respectively. These samples were taken from the market, being all rough stones with a green color. They were transparent, with a bright glass luster (Figures 2 and 3). The crystal morphology of the diopside sample from Pakistani (PKD) was short prismatic, with an idiomorphic grain, and the colors of the individual crystal columns were uneven due to varying levels of local transparency (Figure 2A,B). The crystal surface displayed stepped crystal patterns and raised growth mounds, with the cross sections of the growth mounds being square (Figure 3A,B). The cleavage and fracture in the sample are relatively well developed. When observed under reflected light, distinct internal cleavage flash could be seen from the crystal surface. The healing cracks contained groups of gas–liquid inclusions (Figure 3C). In contrast, the Russian sample (RUS) had a uniform color (Figure 2C,D), with a bright color and high saturation. The crystal morphology was irregular, with conchoidal fractures (Figure 3D,E). The interior of the sample was relatively clean, with fewer visible crystalline inclusions. However, there were more gas–liquid inclusions and cracks in the shape of the beads or fingerprints (Figure 3F).

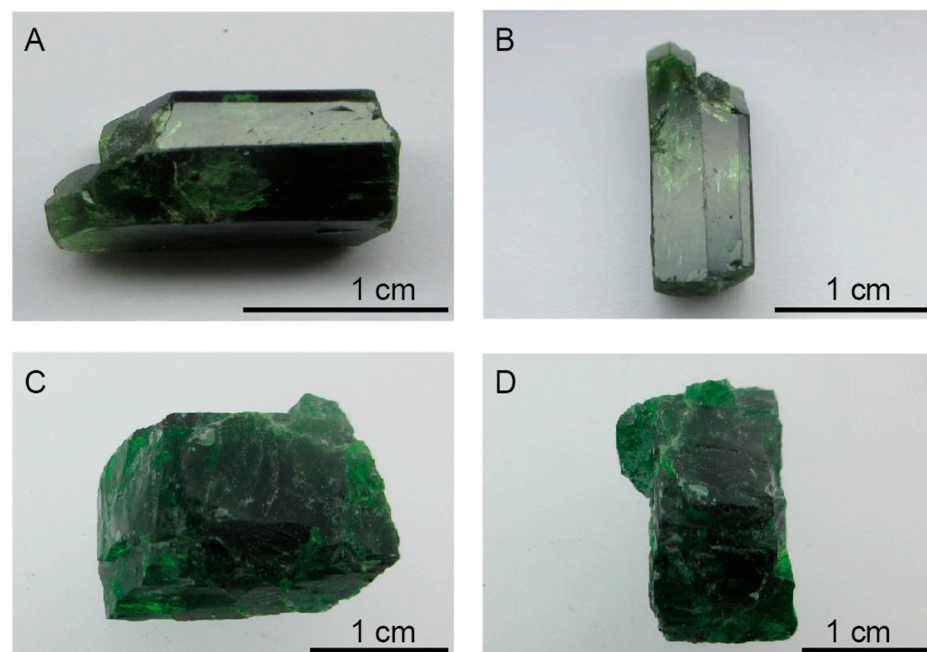


Figure 2. The two diopside rough samples collected and examined for this study: (A,B) Diopside rough sample PKD from Pakistan; (C,D) Diopside rough sample RUS from Russia.

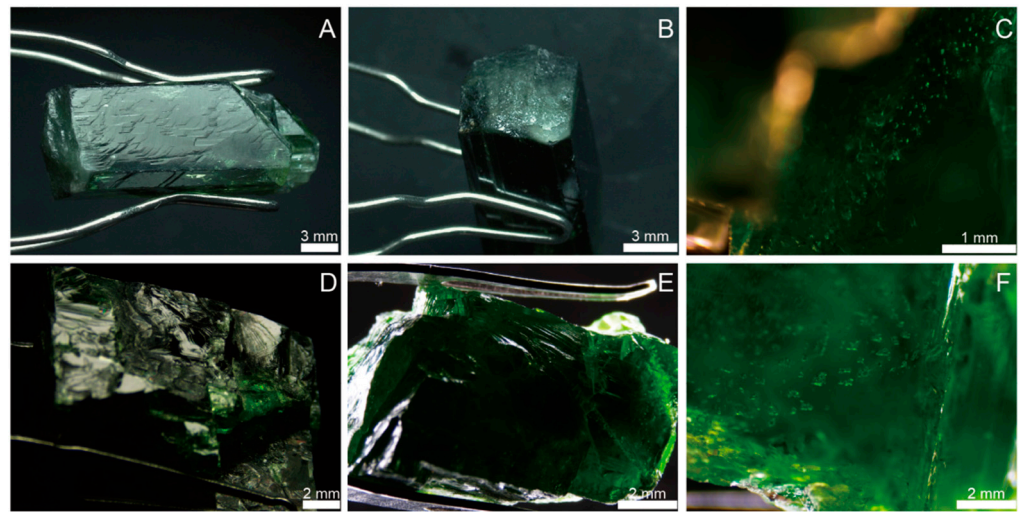


Figure 3. The micrographs of diopside sample PKD (A–C) and RUS (D–F); (A) stepped cleavage formed by two well-defined cleavage planes of PKD diopside sample; (B) fracture perpendicular to *c*-axis of PKD diopside sample; (C) inclusion group within PKD diopside sample; (D,E) conchoidal fractures of RUS diopside sample; (F) inclusion group within RUS diopside sample.

3.2. Microscopic Analysis and Spectroscopy

The gemstone microscopic observation, infrared spectrum, UV-visible spectrum, and laser Raman spectrum were conducted in the Gemological Experimental Teaching Center of School of Gemology, China University of Geosciences (Beijing). Internal and external features were observed with a GI-MP22 gemological photographic microscope using a dark field, bright field, and top illumination.

The infrared spectra were conducted with a Tensor 27 Fourier-transform infrared spectrometer (Bruker, Billerica, MA, USA) using a reflection method. The reflection method conditions were as follows: humidity of less than 70%, scanning voltage of 85–265 V, resolution of 4 cm^{-1} , grating of 6 mm, test range of $400\text{--}2000\text{ cm}^{-1}$, and scanning signal accumulation of 32 times. The UV-visible (UV-VIS) spectroscopy tests were collected from 300 to 800 nm with a UV-3600 UV-VIS spectrophotometer (Shimadzu Corporation, Kyoto, Japan) using a reflection method. A data interval of 2 nm and a scan speed of 405 nm/min were used. An HR-Evolution-type micro-Raman spectrometer (HORIBA, Shimadzu, Kyoto, Japan) was used to perform Raman spectroscopy tests with a 532 nm laser. Raman spectra were collected from $400\text{ to }4000\text{ cm}^{-1}$, with 50 mW of laser power and a resolution of 4 cm^{-1} . The slit width was set to 100 μm , with a grating of 600 gr/mm. The scanning time was 4 s, and the integration time was 3 s.

3.3. SEM Analyses

The two diopside samples were first mechanically crushed, after which the pure parts of the samples were selected under a binocular microscope and placed in an epoxy block to polish it to the largest surface. The polished portions were surface carbon blasted before testing. The backscattered electron (BSE) imaging was performed to observe the structure of diopside samples at the Beijing Gaonianlinghang Company Limited (Beijing, China). The XL30-SFEG electron beam from the company FEI (Eindhoven, The Netherlands) was used for micrographic analysis of diopside samples.

3.4. Chemical Analysis

The electron microprobe analysis was completed in the Experimental Center of the Research Institute of China University of Geosciences (Beijing). The laser ablation–inductively coupled plasma–mass spectrometry (LA-ICP-MS) analysis was carried out at the Institute

of Geomechanics, Chinese Academy of Geological Sciences. All the data results are shown in Tables 1 and 2.

Table 1. Major element composition (wt.%) of diopside samples from Pakistan and Russia by EPMA.

Sample Spots	SiO ₂	TiO ₂	Al ₂ O ₃	FeO	MnO	MgO	CaO	Na ₂ O	K ₂ O	Cr ₂ O ₃	NiO	Total
RUS-01	54.29	0.06	0.42	1.25	0.14	17.37	24.20	0.39	0.03	0.67	0.06	98.88
RUS-02	54.12	0.17	0.29	1.15	0.02	17.81	24.18	0.41	0.01	0.64	0.04	98.84
RUS-03	54.70	0.16	0.24	1.05	0.05	18.25	24.65	0.39	0.01	0.59	0.09	100.19
RUS-04	54.63	0.09	0.25	1.05	0.07	18.19	24.52	0.42	0.02	0.72	0.02	99.98
RUS-05	54.90	0.04	0.22	1.11	0.00	18.20	24.66	0.52	0.04	0.64	0.06	100.37
RUS-06	54.79	0.08	0.23	1.10	0.01	18.30	24.44	0.44	0.02	0.69	0.00	100.09
RUS-07	54.51	0.16	0.24	1.09	0.06	18.10	24.44	0.42	0.01	0.70	0.10	99.82
RUS-08	54.54	0.07	0.23	1.06	0.06	17.85	23.99	0.35	0.01	0.67	0.11	98.92
RUS-09	53.52	0.07	0.25	1.10	0.05	18.33	24.44	0.33	0.02	0.67	0.09	98.85
RUS-10	53.83	0.09	0.23	1.09	0.00	18.47	24.11	0.39	0.01	0.61	0.07	98.88
RUS-11	54.05	0.16	0.33	1.13	0.11	17.97	24.10	0.39	0.02	0.69	0.02	98.97
RUS-12	53.46	0.07	0.32	1.18	0.10	18.19	24.32	0.42	0.03	0.83	0.00	98.93
PKD-01	54.22	0.00	0.49	2.17	0.16	16.95	24.87	0.29	0.00	0.39	0.24	99.78
PKD-02	53.36	0.00	0.52	2.34	0.14	17.05	24.41	0.35	0.01	0.46	0.29	98.91
PKD-03	53.37	0.00	0.41	2.21	0.16	17.33	24.49	0.22	0.01	0.19	0.24	98.63
PKD-04	53.50	0.00	0.44	2.33	0.23	16.96	24.44	0.29	0.00	0.26	0.24	98.70
PKD-05	53.50	0.02	0.44	2.58	0.17	17.32	24.42	0.27	0.01	0.21	0.27	99.20
PKD-06	53.47	0.03	0.47	2.53	0.09	17.38	24.87	0.31	0.00	0.24	0.09	99.47
PKD-07	53.02	0.00	0.49	2.71	0.16	17.26	24.64	0.34	0.00	0.19	0.21	99.02
PKD-08	53.47	0.00	0.46	2.64	0.15	17.33	24.89	0.39	0.03	0.26	0.18	99.81
PKD-09	53.20	0.00	0.68	2.37	0.12	17.08	24.55	0.34	0.01	0.36	0.34	99.04
PKD-10	52.93	0.00	0.16	3.07	0.22	17.41	25.10	0.15	0.01	0.06	0.12	99.23
PKD-11	53.33	0.00	0.16	2.67	0.12	17.37	24.72	0.12	0.01	0.00	0.14	98.65
PKD-12	53.51	0.00	0.14	2.43	0.20	17.61	25.06	0.13	0.02	0.08	0.15	99.31

Sample Spots	Cations on the Basis of 6 Oxygens														T (°C) [34]			
	Si	Ti	Al ^{IV}	Al ^{VI}	Al ^{total}	Fe	Mn	Mg	Ca	Na	K	Cr	Sum	Wo		En	Fs	Mg#
RUS-01	1.991	0.002	0.009	0.009	0.018	0.038	0.004	0.950	0.951	0.028	0.001	0.020	4.003	48.93	48.87	2.20	0.91	1161
RUS-02	1.985	0.005	0.015	0.000	0.013	0.035	0.001	0.974	0.950	0.029	0.000	0.019	4.010	48.48	49.69	1.83	0.92	1159
RUS-03	1.981	0.004	0.019	0.000	0.010	0.032	0.002	0.985	0.956	0.028	0.001	0.017	4.015	48.44	49.88	1.69	0.93	1148
RUS-04	1.981	0.002	0.019	0.000	0.011	0.032	0.002	0.983	0.953	0.030	0.001	0.021	4.016	48.36	49.92	1.73	0.93	1153
RUS-05	1.984	0.001	0.016	0.000	0.009	0.033	0.000	0.981	0.955	0.037	0.002	0.018	4.020	48.50	49.80	1.70	0.93	1107
RUS-06	1.983	0.002	0.017	0.000	0.010	0.033	0.000	0.988	0.948	0.031	0.001	0.020	4.016	48.13	50.16	1.70	0.93	1163
RUS-07	1.982	0.004	0.018	0.000	0.010	0.033	0.002	0.981	0.952	0.030	0.000	0.020	4.014	48.37	49.85	1.77	0.93	1155
RUS-08	1.996	0.002	0.004	0.006	0.010	0.032	0.002	0.974	0.940	0.025	0.000	0.019	4.000	48.27	49.98	1.75	0.93	1188
RUS-09	1.968	0.002	0.032	0.000	0.011	0.034	0.002	1.005	0.963	0.023	0.001	0.019	4.027	48.07	50.16	1.77	0.93	1141
RUS-10	1.975	0.002	0.025	0.000	0.010	0.033	0.000	1.010	0.948	0.028	0.000	0.018	4.023	47.60	50.72	1.68	0.93	1171
RUS-11	1.980	0.004	0.020	0.000	0.014	0.035	0.003	0.981	0.946	0.028	0.001	0.020	4.013	48.14	49.93	1.93	0.92	1171
RUS-12	1.965	0.002	0.035	0.000	0.014	0.036	0.003	0.997	0.958	0.030	0.002	0.024	4.030	48.03	49.99	1.97	0.92	1130
PKD-01	1.985	0.000	0.015	0.006	0.021	0.066	0.005	0.925	0.975	0.020	0.000	0.011	4.009	49.47	46.92	3.62	0.86	
PKD-02	1.974	0.000	0.026	0.000	0.023	0.072	0.004	0.940	0.968	0.025	0.001	0.013	4.020	48.76	47.38	3.86	0.85	
PKD-03	1.977	0.000	0.023	0.000	0.018	0.069	0.005	0.957	0.972	0.016	0.000	0.006	4.019	48.53	47.80	3.67	0.86	
PKD-04	1.982	0.000	0.018	0.001	0.019	0.072	0.007	0.937	0.970	0.021	0.000	0.008	4.015	48.85	47.17	3.98	0.85	
PKD-05	1.974	0.000	0.026	0.000	0.019	0.079	0.005	0.953	0.965	0.020	0.001	0.006	4.023	48.19	47.57	4.24	0.84	
PKD-06	1.967	0.001	0.033	0.000	0.020	0.078	0.003	0.953	0.980	0.022	0.000	0.007	4.030	48.67	47.32	4.00	0.84	
PKD-07	1.964	0.000	0.036	0.000	0.021	0.084	0.005	0.953	0.978	0.025	0.000	0.005	4.035	48.40	47.19	4.41	0.83	
PKD-08	1.965	0.000	0.035	0.000	0.020	0.081	0.005	0.949	0.980	0.028	0.001	0.008	4.036	48.63	47.11	4.26	0.84	
PKD-09	1.968	0.000	0.032	0.000	0.030	0.073	0.004	0.942	0.973	0.024	0.001	0.010	4.025	48.85	47.29	3.86	0.85	
PKD-10	1.961	0.000	0.039	0.000	0.007	0.095	0.007	0.961	0.996	0.011	0.001	0.002	4.040	48.37	46.68	4.95	0.81	
PKD-11	1.978	0.000	0.022	0.000	0.007	0.083	0.004	0.960	0.982	0.009	0.000	0.000	4.023	48.42	47.33	4.26	0.83	
PKD-12	1.972	0.000	0.028	0.000	0.006	0.075	0.006	0.968	0.990	0.009	0.001	0.002	4.029	48.55	47.48	3.97	0.85	

Wo, Ca₂Si₂O₆; En: Mg₂Si₂O₆; Fs: Fe₂Si₂O₆; Mg# = molar Mg/(Mg + Fe^T) × 100.

Major-element compositions were analyzed by an electron probe micro-analyzer (EPMA), JEOL model JXA-8100 (Tokyo, Japan). The analyses were carried out with an accelerating voltage of 15 kV and an electron beam current of 20 nA. Measurement times were set at 10 s for the peak of all analyzed elements and 5 s for the background. The standards used for calibration were NaAlSi₃O₈ (Na), KAlSi₃O₈ (K), Cr₂O₃ (Cr), diopside (Si, Mg, Ca), Fe₂O₃ (Fe), pyrope (Al), Mn₂O₃ (Mn), NiO (Ni), ZnO (Zn), TiO₂ (Ti), and Ca₅P₃F (P) [35,36].

Table 2. Trace element concentrations (ppm) of diopside samples from Pakistan and Russia by LA-ICP-MS.

Sample Spots	Li	Be	B	Sc	V	Cr	Ni	Zn	Ga	Ge	As	Rb	Sr	Y	Zr	Cd	Sn
PKD-01	19.6	1.71	6.31	1.67	17.8	2658	2395	107	0.537	1.46			10.5		0.406		0.250
PKD-02	21.1	2.05	6.36	1.79	18.2	2552	2406	117	0.471	1.43	0.221	0.282	10.8		0.564	0.0273	0.368
PKD-03	21.2	1.90	7.36	2.24	18.9	2330	2237	115	0.539	0.605	0.0581		11.2		0.203	0.0956	0.532
PKD-04	21.4	1.98	8.16	1.79	18.3	2824	2558	121	0.676	0.855		0.301	11.4	0.0233	0.226	0.246	0.250
PKD-05	16.8	1.44	7.56	2.13	19.3	1962	2214	129		1.25	0.605		9.63		0.407	0.137	
PKD-06	12.2	1.32	7.44	2.21	20.5	1569	2074	135		0.576			11.0	0.0235	0.317	0.219	0.222
PKD-07	12.1	1.35	7.63	2.39	20.3	1547	2036	148		1.21	0.197	0.177	11.0		0.360		0.263
PKD-08	12.1	1.21	7.38	2.28	19.7	1507	2001	139	0.633	0.774			9.25		0.314	0.271	0.191
PKD-09	15.2	1.92	7.59	1.40	20.0	1803	2306	121	0.463	1.47	0.359	0.336	12.0	0.0116	0.357	0.259	0.163
PKD-10	7.83	0.321	3.26	6.51	8.82	235	805	112		0.580	0.197	0.388	11.5	0.128	0.400		0.325
PKD-11	10.6	0.870	3.47	3.42	11.5	150	1231	99.1	0.0325	1.13	0.0462		14.42	0.0347	0.111		0.255
PKD-12	9.18	0.981	3.21	2.83	10.3	157	1188	108	0.323	1.53	0.0115	0.229	13.4	0.0346	0.110	0.209	0.0416
RUS-01	0.570	0.072	2.70	68.5	7.19	5079	257	10.8	0.978	4.45	0.358		2149	5.37	8.59		0.386
RUS-02	0.372	0.029	2.99	68.0	7.33	4993	250	8.76	0.921	4.28	0.637		2150	5.45	8.81	0.102	0.439
RUS-03	1.31	0.130	2.55	57.0	5.91	4060	249	10.9	0.630	3.39	0.603	0.0531	2065	3.73	3.91	0.0868	0.479
RUS-04	1.41	0.130	3.15	67.6	6.90	4585	257	9.46	1.10	3.65	0.476		2042	4.99	5.65	0.158	0.564
RUS-05	1.65	0.130	2.54	68.6	6.81	4644	260	10.6	0.843	4.51	0.721		2183	5.62	7.02	0.156	0.445
RUS-06	1.42	0.188	1.58	69.9	7.31	4877	260	10.6	0.544	2.62	0.781		2229	6.10	7.77	0.0841	0.279
RUS-07	2.21	0.175	2.32	61.9	6.43	5095	251	10.4	1.06	2.66	0.210	0.446	2307	4.25	5.65		0.283
RUS-08	1.97	0.161	2.69	63.5	6.72	5190	260	9.12	1.22	4.30	0.432		2312	4.54	6.55		0.622
RUS-09	2.42	0.146	2.87	58.5	5.81	4051	226	9.12	0.608	3.80	0.304		2240	4.33	5.90	0.0828	0.151
RUS-10	1.38	0.103	2.35	63.4	6.51	4479	257	11.9	1.28	2.83			1897	4.19	5.83	0.110	0.227
RUS-11	1.13	0.147	3.25	66.7	7.42	4685	238	10.8	1.58	2.16	0.105		2120	5.95	9.57		0.278
RUS-12	1.26		2.86	70.2	7.72	4786	248	9.54	1.24	3.41	0.234	0.160	1916	5.75	9.76	0.0965	0.504

Sample Spots	Ba	La	Ce	Pr	Nd	Sm	Eu	Gd	Tb	Dy	Ho	Er	Tm	Yb	Lu	Hf	Pb (Total)
PKD-01	0.101								0.0108			0.0315		0.1553		0	0.545
PKD-02		0.0128	0.0123		0.0616	0.0732			0.0108	0.0428	0.0112		0.021	0.0522	0.0119	0	0.389
PKD-03		0.0129	0.0248			0.0737			0.0109	0.0432			0.0106			0.1206	0.416
PKD-04	0.205	0		0.0203		0.0741		0.0719								0.0403	0.475
PKD-05		0.0392	0.0126			0.0746						0.0322	0.0107			0	0.373
PKD-06							0.0207		0.011		0.0115	0.0324				0	0.465
PKD-07			0.0126							0.0888		0.0322	0.0215	0.0536		0.0408	0.35
PKD-08		0.013			0.0626		0.0413							0.0532		0	0.373
PKD-09			0.05				0.0206				0.0342	0.0318	0.0107		0.0121	0.0407	0.444
PKD-10	0.103		0.0124	0.0306		0.0731				0.0435	0.0341		0.0107	0.1048	0.012	0.0813	0.459
PKD-11	0.309		0.0124					0.0715							0.024	0.0406	0.393
PKD-12										0.0429			0.0107			0.0406	0.343
RUS-01	1.93	7.19	19.1	3.02	15.2	2.88	1.02	2.94	0.319	0.812	0.247	0.375	0.107	0.463	0.0837	0.77	0.897
RUS-02	1.21	6.47	19.6	2.71	15.6	4.05	1.22	2.72	0.22	1.33	0.281	0.532	0.0745	0.465	0.0957	0.486	0.824
RUS-03	1.81	6.37	16.7	2.6	15.2	2.83	0.877	2.57	0.329	0.813	0.191	0.376	0.0426	0.414	0.0958	0.283	0.823
RUS-04	0.8	6.8	19.2	3.17	14.8	3.56	1.08	3.11	0.219	1.03	0.281	0.314	0.0958	0.572	0.0958	0.606	0.838
RUS-05	2.09	6.65	20.3	2.65	14.7	2.41	1.21	2.34	0.153	0.943	0.315		0.0426	0.469	0.0719	0.404	0.727
RUS-06	1.09	7.4	21.3	2.93	15.9	3.66	0.961	3.5	0.338	1.33	0.169	0.631	0.128	0.575	0.06	0.726	0.797
RUS-07	1.68	7.06	18.8	2.93	13.1	3.44	0.899	1.91	0.119	1.15	0.246	0.378	0.0211	0.573	0.0476	0.32	0.775
RUS-08	1.89	6.68	18	2.53	13.3	3.14	0.898	2.73	0.258	1.58	0.167	0.314	0.0738	0.623	0.0829	0.438	0.835
RUS-09	1.99	5.95	16.4	2.34	10.7	2.99	0.673	1.84	0.246	0.51	0.177	0.251	0.042	0.414	0.059	0.278	0.763
RUS-10	1.6	6.7	18.9	2.54	14.2	3.35	1.24	2.53	0.245	1.14	0.199	0.406	0.0419	0.309	0.047	0.277	0.714
RUS-11	1.3	6.85	19.8	3	14.5	4.58	1.02	2.12	0.254	1.65	0.198	0.468	0.073	0.205	0.129	0.669	0.75
RUS-12	2.11	7.28	20.2	2.78	16.2	4	1.12	3.28	0.264	1.31	0.286	0.435	0.0624	0.46	0.116	0.588	0.771

LA-ICP-MS was applied to analyze the trace element concentrations, using a 193 nm excimer laser ablation system (GeoLas HD; Coherent, Santa Clara, CA, USA), and a four-stage rod mass spectrometer (Agilent 7900, Agilent Technologies, Tokyo, Japan) was used for inline testing, with Ar and He as the carrier gases. The laser employed a 10 Hz pulse rate and a 35 μm diameter spot size. The energy density was about 9 J/cm². NIST-SRM 610 and 612 glasses reference materials were used as external calibration standards. Data reduction was carried out using the software Iolite to analyze the following elements: Li, Be, Ti, V, Cr, Mn, Fe, Co, Ni, Cu, and Zn [37].

4. Results

4.1. Visual Appearance and Gemological Properties of Diopside

The two diopside samples from Pakistan and Russia were a green uniform color, with a transparent and glassy luster (Figure 3). The PKD diopside sample showed a stepped cleavage with two well-defined cleavage planes (Figure 3A). The RUS diopside sample had greasy and shiny conchoidal fractures (Figure 3D,E). Gemstone microscopic observation showed that there were inclusion groups and fractures in both of the diopside samples. They all had lamellar gas–liquid groups and partially healed fissures (Figure 3C,F).

4.2. Spectral Characteristics

4.2.1. FTIR Spectrum

The representative FTIR spectrums of the diopside samples from Pakistan and Russia are shown in Figure 4. The infrared spectra of the two diopside samples in the range of 4–1200 cm^{-1} are relatively similar. In general, no reflectance bands are observed above 1500 cm^{-1} , which suggests the absence of OH groups or water molecules in these crystalline phases.

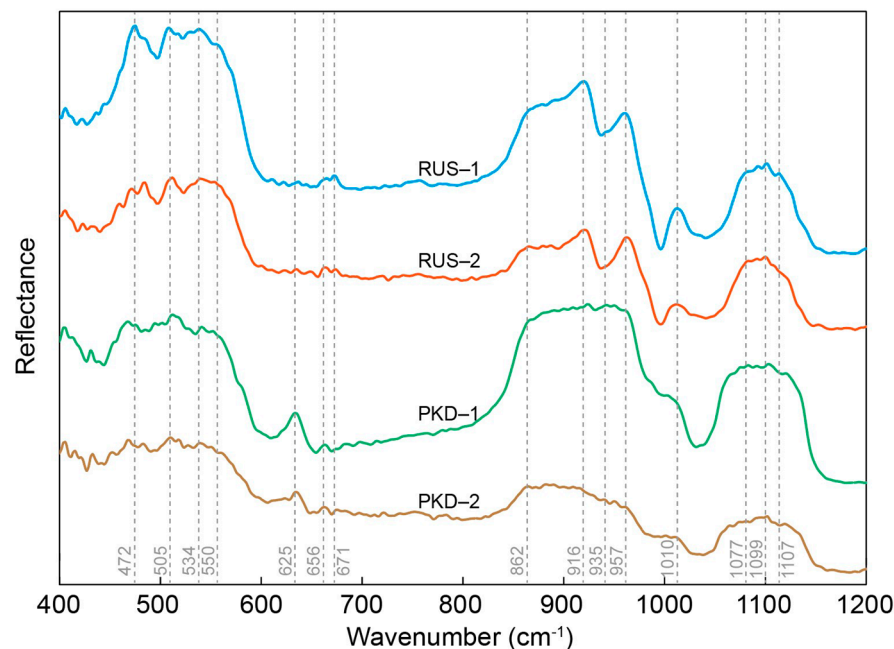


Figure 4. FTIR spectrum for the 400–1200 cm^{-1} frequency range, obtained from PKD and RUS diopside samples.

According to the literature on diopside, the infrared spectrum vibration of diopside is mainly manifested in the characteristic Si–O stretching modes, non-bridging stretching modes of Si–O, and the non-bridging bending vibrations of the O–Si–O of a SiO_4 tetrahedron [38–42]. All the detected bands were in good agreement with the vibrations of the functional groups of diopside. Seven weak absorption peaks at around 472 cm^{-1} , 505 cm^{-1} , 534 cm^{-1} , 550 cm^{-1} , 625 cm^{-1} , 656 cm^{-1} , and 671 cm^{-1} were assigned to the bending vibrations of the non-bridging bending vibrations of the O–Si–O of a SiO_4 tetrahedron. The broad absorption band around 862 cm^{-1} and the broad absorption band in the range of 900–1100 cm^{-1} (including 916 cm^{-1} , 935 cm^{-1} , 957 cm^{-1} and 1100 cm^{-1}) were assigned to the non-bridging stretching modes of Si–O and the characteristic Si–O stretching modes of the SiO_4 tetrahedron, respectively. The infrared spectra of the diopside samples from Pakistan and Russia tended to be consistent, and only some absorption peaks were slightly offset, which could be due to different orientations of the diopside crystals within the gem or to variations in the elemental compositions of non-stoichiometric diopside phases.

4.2.2. Raman Spectra

The Raman spectra of pyroxene silicates are characterized by four types of vibration bands: (1) Si–O nonbridging stretching (Si-O_{nbr}); (2) Si–O bridging stretching (Si-O_{br}); (3) O–Si–O bending; and (4) cation M1- and M2-oxygen vibration modes (M–O). The stretching modes of Si-O_{nbr} are observed in the spectra at frequencies higher than the modes of Si-O_{br} due to a stronger force constant, i.e., the coefficient that links the displacement of atoms from their equilibrium position with the force that such displacement induces on adjacent atoms [43–47].

The Raman spectra of the diopside samples from Pakistan and Russia showed sharp spectrum peaks and high signal-to-noise ratios (Figure 5). The Raman spectra of the diopside samples from Pakistan and Russia exhibited remarkable similarities to each other, as well as to those previously reported on in the literature [45,47], and only the intensity and wavenumber of each Raman scattering peak feature were slightly different. There were four evident peaks within the range of 100–1200 cm^{-1} , respectively, 322 cm^{-1} , 389 cm^{-1} , 666 cm^{-1} , and 1012 cm^{-1} . The 322 cm^{-1} and 389 cm^{-1} figures were caused by the cation–oxygen vibrations. The 666 cm^{-1} figure was the stretching of Si-O_{br} bonds, and 1012 cm^{-1} corresponded to the Si-O_{nbr} stretching mode [45,48]. The Pakistan diopside sample showed a high Raman scattering peak intensity of 141 cm^{-1} , while the diopside sample from Russia was relatively weak. The Raman scattering peaks of the diopside samples from Pakistan and Russia showed the same positions but different intensities, which may be caused by the variation in the cation occupancy in the M sites. In other words, the lattice vibration involving Mg should also affect Raman spectrum characteristics of the diopside samples in the range of 326–393 cm^{-1} , leading to the difference in the intensities of the Raman scattering peaks [45].

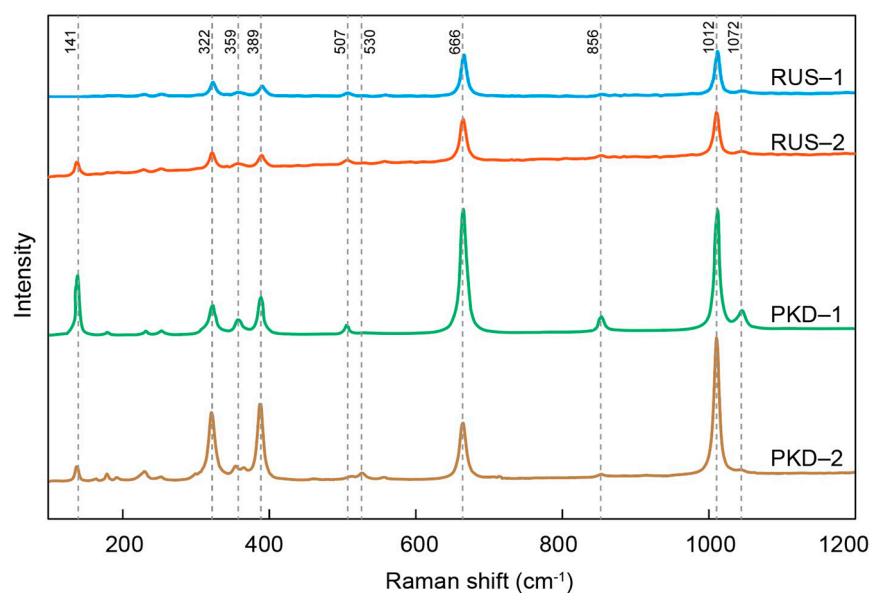


Figure 5. The representative Raman spectrum of the diopside samples.

4.2.3. UV-Visible Spectra

The UV-VIS spectra of the diopside samples from Pakistan and Russia showed similar patterns, as illustrated in Figure 6. The UV-VIS spectrum revealed that the diopside samples had significant reflections at 460–470 nm and 655–665 nm. The 460–470 nm and 655–665 nm reflections were attributed to Cr^{3+} in octahedral coordination [41,49]. The diopside samples from Pakistan and Russia had weak reflections between 230 nm and 285 nm, which were caused by the intervalence Fe^{2+} – Fe^{3+} charge transfer [40,41,49].

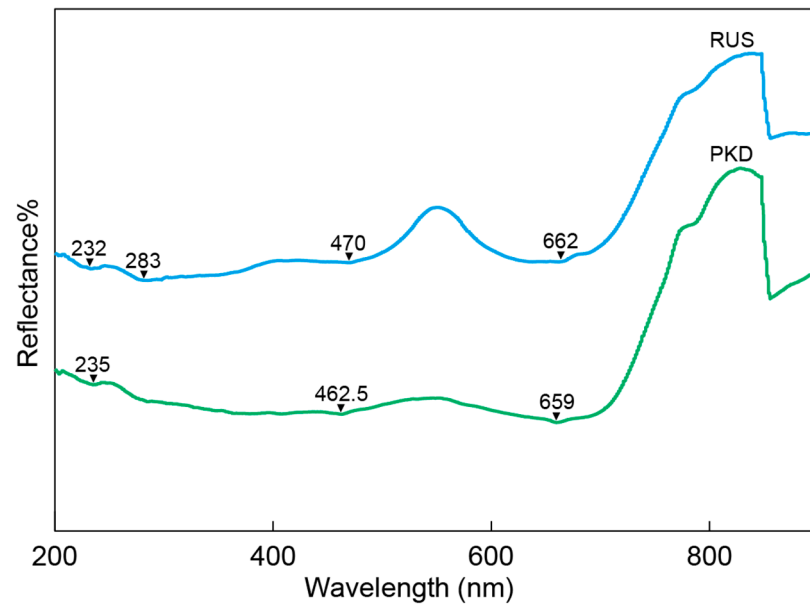


Figure 6. The representative UV-Vis-NIR spectrum of the diopside samples.

4.3. Major and Trace Elements Characteristics of Diopside

The compositions of major elements and trace elements of the diopside samples from Pakistan and Russia are presented in Tables 1 and 2, respectively. The diopside samples contained <5 mol.% ferrosilite (Fs). In the En–Wo–Fs classification diagram [50], they are all localized in the diopside corner (Figure 7A,B). We analyzed the major and trace elements of the diopside samples at the same positions, including the core and rim of the diopside crystals. There was no evident difference in the elements' characteristics between the core and rim of the same diopside sample. Meanwhile, the backscattered electron images of the diopside samples from Pakistan and Russia also showed no zoned features (Figure 7C,D).

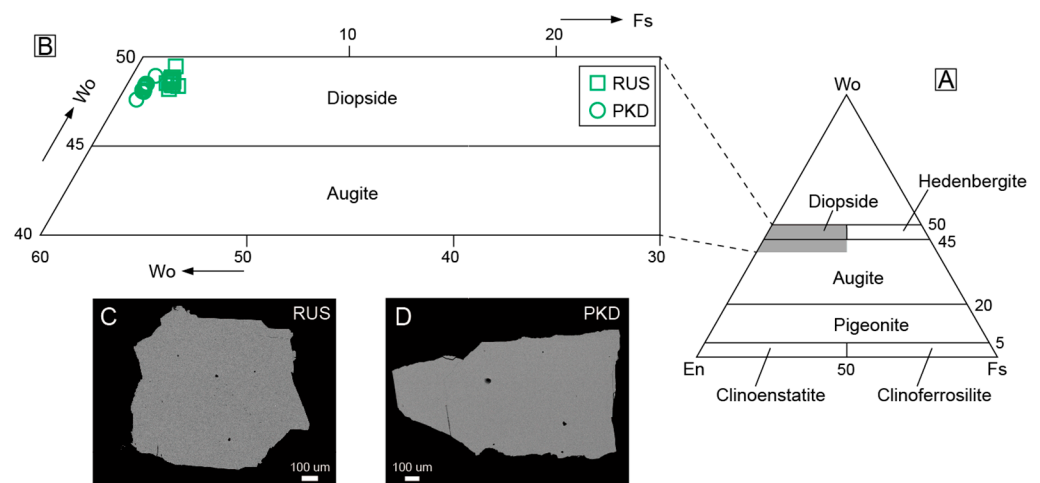


Figure 7. (A) The diagram of pyroxene classification based on En–Wo–Fs compositions for the diopside samples; (B) partial Enlargement of the En–Wo–Fs composition diagram (A); (C,D) backscattered electron images of the Pakistan and Russia diopsides.

The diopside sample from Russia had higher Mg# (91–93; Mg# = molar Mg/(Mg + Fe^T) × 100), SiO₂ (53.5–54.9 wt.%), Na₂O (0.33–0.52 wt.%), and lower CaO (24.0–24.7 wt.%), while the diopside sample from Pakistan had relatively lower Mg# (81–86), SiO₂ (52.9–54.2 wt.%), Na₂O (0.12–0.39 wt.%), and higher CaO (24.4–25.1 wt.%).

The major elements of the diopsides with different geographic origins showed great differences (Figure 8; Table 1).

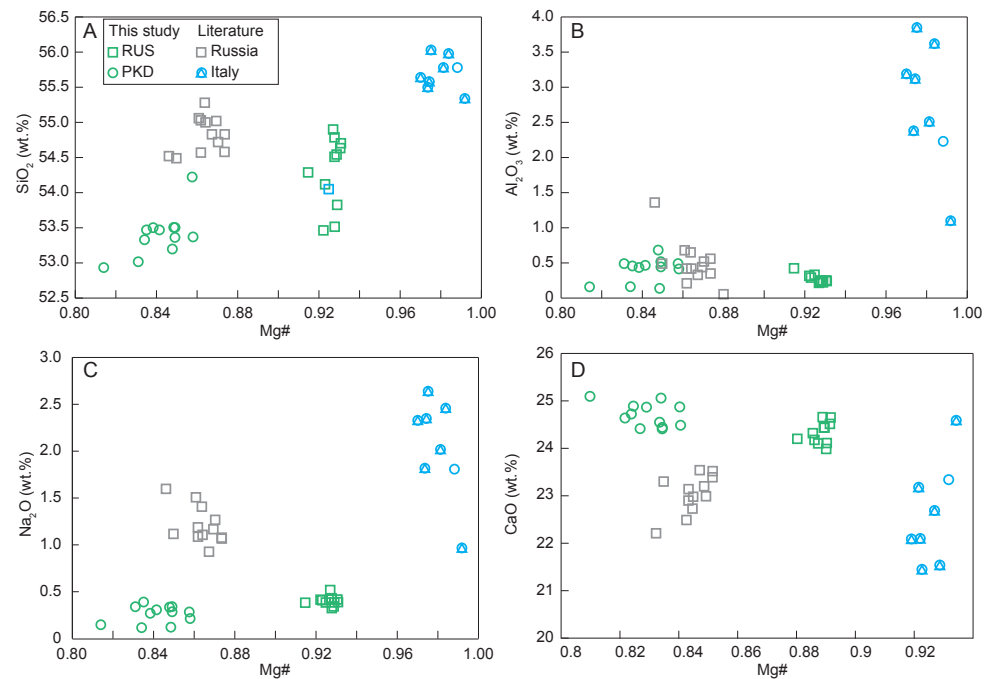


Figure 8. Variation diagrams of Mg# vs. (A) SiO₂; (B) Al₂O₃; (C) Na₂O; (D) CaO for the diopside samples.

The diopside sample from Russia displayed significantly higher concentrations of Cr, Zr, Sr, and Sc compared with the Pakistan diopside sample (Table 2). Investigating the distribution patterns of rare earth elements (REEs) can be used as a very valuable tool to determine phyrochemical conditions and the origin of minerals and rocks [51]. Notably, the chondrite-normalized REE diagrams revealed discernible differences between the Pakistan and Russia diopside samples (Figure 9). The diopside sample from Russia had a greater abundance of REE, was particularly enriched in light rare earth elements (LREEs), with no Eu anomalies, and had low levels of heavy rare earth element (HREE) contents. Conversely, the diopside sample from Pakistan displayed extremely low REE contents (Figure 9; Table 2).

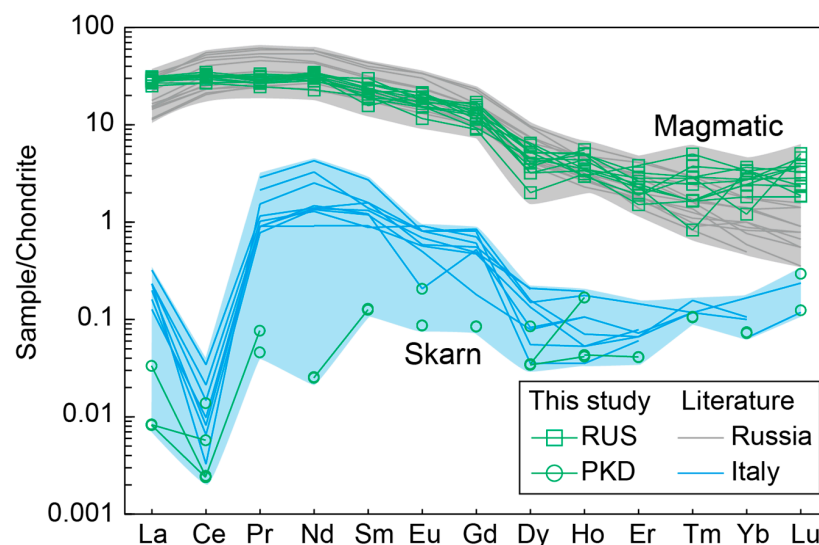


Figure 9. Chondrite-normalized REE patterns for the diopside samples. The grey and blue areas represent the diopsides from magmatic and skarn processes, respectively.

5. Discussion

5.1. Gemological Characteristics

The diopside sample from Russia (RUS) exhibited remarkable characteristics of high transparency, a strong luster, and a bright green color with yellow tones. The transparency of the Pakistan diopside sample (PKD) was relatively modest, with shades of emerald-green that bore a resemblance to the Russian diopside sample. The Pakistani diopside sample had been subjected to an irregular configuration of crystal particles, alongside impurities that impeded its transparency levels, giving it a semi-translucent, micro-transparent appearance. Notably, the luster of diopside samples from Pakistan and Russia exhibited little variation.

The diopside samples from Pakistan and Russia exhibited color stabilities under the Charles filter. The Russian sample, however, displayed a visible red absorption band of Cr^{3+} under spectroscopic examination. Conversely, the Pakistan sample showed only a combined absorption band of $\text{Fe}^{2+}/\text{Fe}^{3+}$ or $\text{Fe}^{2+} + \text{Fe}^{3+}$. Additionally, both samples displayed almost no reaction under ultraviolet fluorescence, which was likely due to the presence of Fe content within the samples. The refractive indexes of the diopside samples from Pakistan and Russia, after being polished and ground, were measured using a refractometer. The results revealed that the refractive indexes for the two diopside samples ranged between 1.68 and 1.69. The average refractive index for the diopside sample from Pakistan was slightly higher than that of the Russian diopside sample. This variance in refractive index was attributed to the Fe content in the diopside samples, as the Russian samples possessed lower Fe content than that of the Pakistan sample (Table 1).

5.2. Chromogenic Mechanism of Different Diopsides

The chemical composition of diopside is $\text{CaMg}[\text{Si}_2\text{O}_6]$. Ca^{2+} and Mg^{2+} could be often replaced by Fe^{3+} , Fe^{2+} , V^{3+} , Cr^{3+} , Mn^{2+} , and other transition metal ions, which are known as “chromophores” and are considered to play a significant role on the color characteristics. In this study, we give a certain explanation for the chromogenic mechanism of diopsides of different colors, according to the characteristics of their chemical compositions.

We collected the chemical compositions of the blue diopsides from Saint Marcel (Val D’Aosta, Italy) to compare with the diopside samples from Pakistan and Russia in this study [15,16]. The collected diopside data from the Zagadochnaya kimberlite (Yakutia, Russia) had no color information, and they also were not gem-quality diopside; thus, these data were excluded from the study of chromogenic mechanism [15].

The transition elements contained in these blue and green diopsides were mainly Cr, Mn, Fe, Co, Ni, and V. The Ti and REE contents of the diopsides in different colors cannot be distinguished, suggesting they had no decisive effect on chromogenesis. As shown in Figure 10, the green hue observed in the diopside samples could be explained by their enrichment in Cr, Fe, V, and Ni, with respect to the blue diopside samples. Mn and Co contents could be related to the blue hue of the diopside; the blue diopside samples from Italy had higher Mn and Co contents compared with the green diopsides (Figure 10).

In summary, our new data showed that the behavior of major and trace elements played a significant role in the color differences of diopside crystals. The diopside was colored blue to green by Cr and Fe, respectively, both substituting for Al and Mn in the structure (Figure 11). Meanwhile, the enrichment of V and Ni instead of Co in the trace elements made the diopside present green rather than blue (Figure 10).

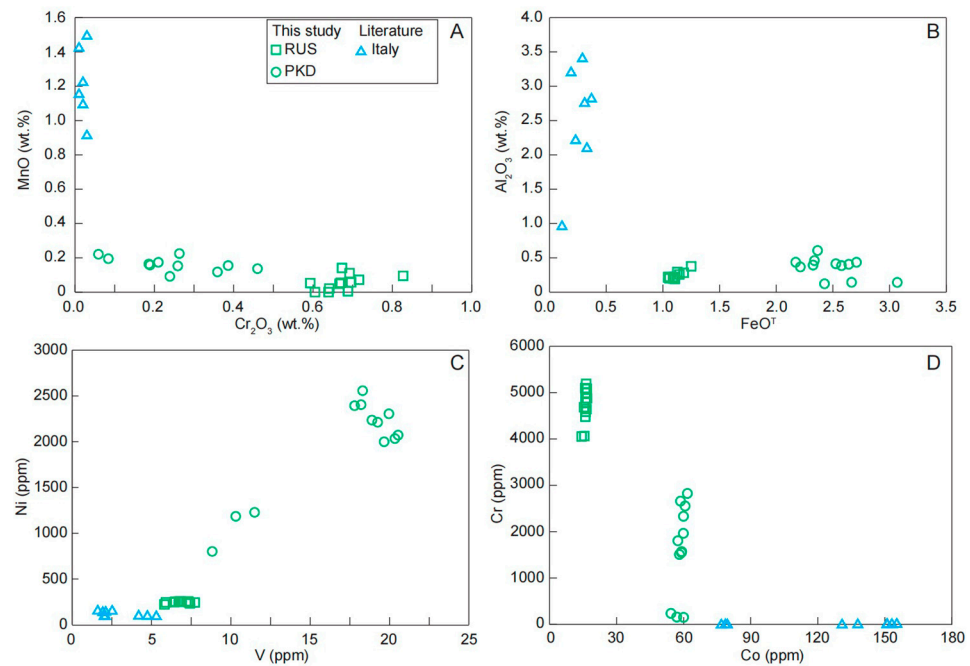


Figure 10. Variation diagrams of (A) Cr_2O_3 vs. MnO ; (B) FeO^{T} vs. Al_2O_3 ; (C) V vs. Ni ; (D) Co vs. Cr for the diopside samples.

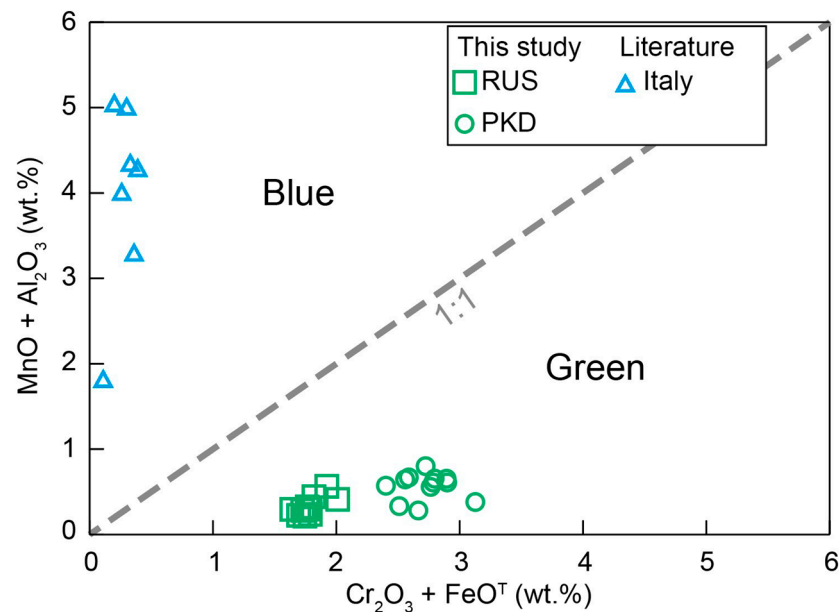


Figure 11. Variation diagrams of $\text{Cr}_2\text{O}_3 + \text{FeO}^{\text{T}}$ vs. $\text{MnO} + \text{Al}_2\text{O}_3$ for the diopside samples.

5.3. Origin of Different Diopsides: Elemental Constraints

Combining the collected diopside data from Saint Marcel (Val D'Aosta, Italy) and the same region in Russia, as well as the data in this study, we can see the distinct characteristics of the contrasting trace element patterns and the chondrite-normalized REE (Figures 9 and 12) [15,16]. The diopside samples from Russia exhibited higher Sc, Zr, Sr, and REE contents than those of the Pakistan and Italy diopside samples (Figures 9 and 12), which could be well explained by the distinct formation processes of the two categories of diopside samples with different origins. The diopside samples from Russia formed from the magmatic evolution process of ultrabasic rocks and crystallized as a basic mineral at the early stages. The overall compositions of the diopsides from Russia remained relatively uniform,

indicating their crystallization in a similar magma system. They had higher Cr, Sc, Zr, Sr, and REE, which were close to the composition of volcanic clinopyroxene in basalt magma [52,53].

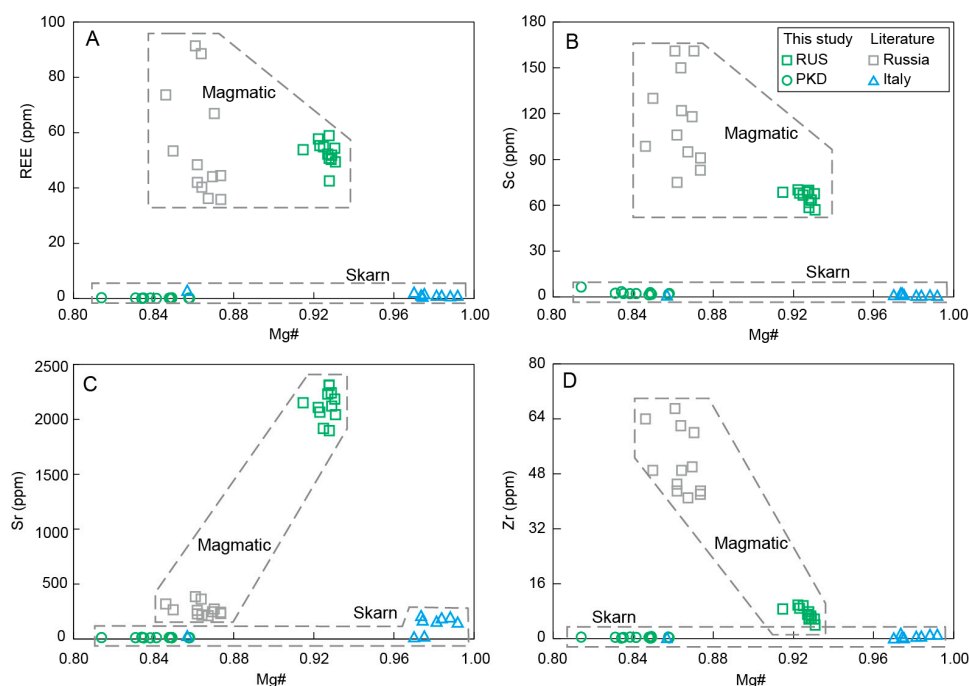


Figure 12. Variation diagrams of Mg# vs. (A) REE, (B) Sc, (C) Sr, and (D) Zr for the diopside samples.

Clinopyroxene is commonly present in igneous rocks and exhibits large compositional variations. Numerous thermometers that utilize clinopyroxene composition have been established and widely applied in magmatic systems, due to their compositional sensitivity to changes in temperature [54–57]. The clinopyroxene-only thermometer is one of the most practical tools to reconstruct crystallization temperatures of clinopyroxenes because it does not require any information of coexisting melts or other co-crystallized mineral phases. Thus, an updated clinopyroxene-only thermometer was used for the diopside sample from Russia in this study and the collected diopside data from Russia, which yielded uncertainties in the estimated temperature (± 37 °C) [15,34], returning crystallization temperature conditions of 1107–1188 °C and 1108–1166 °C, respectively (Figure 13). These similar crystallization temperatures also confirmed that they formed at similar magmatic crystallization stages, similar to the early stage of alkaline ultrabasic magma.

The collected diopside data from Russia exhibited comparably low Mg# in contrast to those of the diopside sample from Russia in this study, indicating the relatively latter crystallization process of the collected Russian diopsides, which was further proved by their lower crystallization temperatures (Figures 8 and 13). The Sc and Zr, as incompatible elements within the magma evolution process, showed an upward trend in conjunction with the decrease in Mg# (Figure 12B,D). Conversely, the Sr content of diopsides from Russia gradually declined as the Mg# decreased (Figure 12C), suggesting that the crystallization of plagioclase, which is rich in Sr, had occurred with diopside crystallization, resulting in a significant depletion of Sr in the residual melt [58–61]. The relatively high concentration of the REE in alkaline ultrabasic magma rendered the diopside from Russia to have a notable REE contents, with comparable REE distribution characteristics (Figure 9).

The diopside sample from Pakistan shared similar composition characteristics with the diopsides from Italy, produced in the skarn metamorphism process. They all had very low Sc, Zr, Sr, and REE contents (Figure 12) and exhibited similar REE characteristics, which were significantly different from the Russian diopside produced during magmatic processes (Figure 9) [60–65]. These suggested that the diopside sample from Pakistan also crystallized within the skarn metamorphism process.

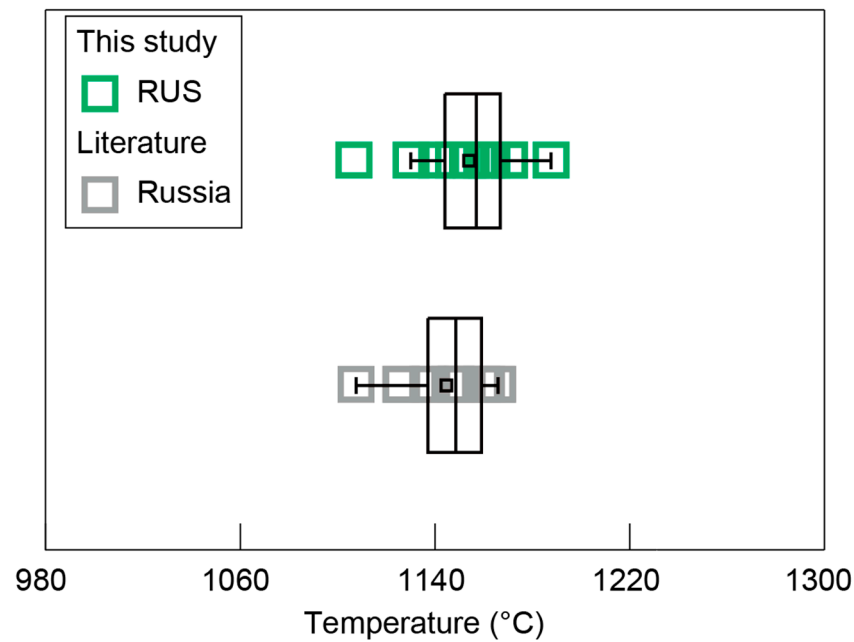


Figure 13. Temperature results for the diopside samples from Russia.

In summary, the elemental characteristics of the diopside samples could well distinguish the distinct formation processes of different diopsides from Russia and Pakistan (Figures 9 and 12). The diopsides from Russia crystallized in the early stages of the ultrabasic magma evolution process, while the diopsides from Pakistan crystallized during the process of skarn metamorphism.

6. Conclusions

We have investigated the gemological characteristics of diopside samples from Pakistan and Russia and analyzed their infrared spectra, Raman spectra, ultraviolet spectra, and chemical compositions. The results were used to present a comprehensive report on their systematic mineralogical characteristics and to discuss the differences in the chromogenic mechanisms and origins of the diopsides. The diopsides from Russia and Pakistan had similar gemological characteristics. The green hue of the diopside was due to chromophore elements such as Cr, Fe, V, and Ni, while the blue color could be attributed to the Al, Mn, and Co elements. The green diopside sample from Pakistan crystallized during the skarn metamorphic process, and the Russian green diopside crystallized at an early stage of the ultrabasic magma evolution process. These findings provided valuable insights into how the diopsides were formed, along with the geological histories and mineralogies of these two regions. These diopside samples showed well-developed crystals without any zoning in BSE images, which enhanced their scientific value and made them suitable as standard samples for further research.

Author Contributions: Writing—original draft, Z.W.; writing—review and editing, Z.W., X.H. and B.X.; data curation, Z.W. and J.R.; methodology, Z.W. and X.H. All authors have read and agreed to the published version of the manuscript.

Funding: This research was funded by the National Natural Science Foundation of China (42222304, 42073038, 41803045, 42202081), the Young Talent Support Project of CAST, the Fundamental Research Funds for the Central Universities (Grant No. 265QZ2021012), and IGCP-662.

Data Availability Statement: The data presented in this study are available within the article.

Acknowledgments: We thank the editor and reviewers for their constructive comments, which helped in improving our paper. This is the 14th contribution of B.X. from the National Mineral Rock and Fossil Specimens Resource Center.

Conflicts of Interest: The authors declare no conflict of interest.

References

1. Cameron, M.; Sueno, S.; Prewitt, C.T.; Papike, J.J. High-temperature crystal chemistry of acmite, diopside, hedenbergite jadeite, spodumene and ureyite. *Am. Mineral. J. Earth Planet. Mater.* **1973**, *58*, 594–618.
2. Putnis, A. *An Introduction to Mineral Science*; Cambridge University Press: Cambridge, UK, 1992.
3. Titorenkova, R.; Kostov-Kytin, V.; Dimitrov, T. Synthesis, phase composition and characterization of Co-diopside ceramic pigments. *Ceram. Int.* **2022**, *48*, 36781–36788. [[CrossRef](#)]
4. Akasaka, M.; Takasu, Y.; Handa, M.; Nagashima, M.; Hamada, M.; Ejima, T. Distribution of Cr³⁺ between octahedral and tetrahedral sites in synthetic blue and green (CaMgSi₂O₆)₉₅(CaCrAlSiO₆)₅ diopsides. *Mineral. Mag.* **2019**, *83*, 497–505. [[CrossRef](#)]
5. Mantovani, L.; Tribaudino, M.; Bertoni, G.; Salviati, G.; Bromiley, G. Solid solutions and phase transitions in (Ca, M²⁺)M²⁺Si₂O₆ pyroxenes (M²⁺ = Co, Fe, Mg). *Am. Mineral.* **2014**, *99*, 704–711. [[CrossRef](#)]
6. White, W.B.; Mccarthy, G.J.; Scheetz, B.E. Optical spectra of chromium, nickel, and cobalt-containing pyroxenes. *Am. Mineral. J. Earth Planet. Mater.* **1971**, *56*, 72–89.
7. Mottana, A.; Rossi, G.; Kracher, A.; Kurat, G. Violan revisited: Mn-bearing omphacite and diopside. *TMPM Tschermaks Mineral. Petrogr. Mitt.* **1979**, *26*, 187–201. [[CrossRef](#)]
8. Griffin, W.L.; Mottana, A. Crystal chemistry of clinopyroxenes from the St. Marcel manganese deposit, Vald'Aosta, Italy. *Am. Mineral.* **1982**, *67*, 568–586.
9. Lin, C.Y.; Zhu, H.B.; Wang, Z.M.; Xie, H.S.; Zhang, Y.M.; Xu, H.G. Optical absorption spectra and colors of jadeites and diopsides. *Acta Mineral. Sin.* **1988**, *3*, 193–199, (In Chinese with English Abstract).
10. Yuan, Y.M.; Qiu, X.J. Optical absorption spectra of diopside. *Acta Mineral. Sini.* **1985**, *2*, 157–184, (In Chinese with English Abstract).
11. Cara, W.; Laurs, B.M. Blue diopside from Russia. *J. Gemmol.* **2020**, *37*, 124–126.
12. Korchagin, A.M. *Inagli Pluton and Its Mineral Resources*; Nedra: Moscow, Russia, 1996; Volume 157. (In Russian)
13. Naumov, V.; Kamenetsky, V.; Thomas, R. A record of alkali silicate-sulphate melts trapped as inclusions in chromium diopside (Inagty deposit, Yakutia, Russia). In Proceedings of the Program with Abstracts of the First Meeting Asia Current Research on Fluid Inclusion, Asian Current Research on Fluid Inclusions I, Nanjing, China, 26–28 May 2006.
14. Okrugin, A.V.; Borisenko, A.S.; Zhuravlev, A.I.; Travin, A.V. Mineralogical, geochemical, and age characteristics of the rocks of the Inagli dunite–clinopyroxenite–shonkinite massif with platinum–chromite and Cr-diopside mineralization (Aldan Shield). *Russ. Geol. Geophys.* **2018**, *59*, 1301–1317. [[CrossRef](#)]
15. Khlif, N.; Vishnevskiy, A.; Izokh, A.; Chervyakovskaya, M. Mineral Chemistry and Trace Element Composition of Clinopyroxenes from the Middle Cambrian Ust'-Sema Formation Ankaramites and Diopside Porphyry Basalts and the Related Barangol Complex Intrusions, Gorny Altai, Russia. *Minerals* **2022**, *12*, 113. [[CrossRef](#)]
16. Diella, V.; Bocchio, R.; Caucia, F.; Marinoni, N.; Langone, A.; Possenti, E. New insights for gem-quality Mn-bearing diopside-omphacite, violane variety, from Saint Marcel (Val D'Aosta, Italy): Its trace elements and spectroscopic characterization. *Minerals* **2021**, *11*, 171. [[CrossRef](#)]
17. Le Fort, P.; Pecher, A. An Introduction to the geological Map of the Area between Hunza and Baltistan, Karakorum–Kohistan–Ladakh–Himalaya Region, Northern Pakistan (Scale 1:150,000). *Geologica* **2002**, *6*, 1–140.
18. Agheem, M.H.; Shah, M.T.; Khan, T.; Murata, M.; Dars, H.; Zafar, M. Petrogenetic evolution of pegmatites of the Shigar valley, Skardu, Gilgit–Baltistan, Pakistan. *Arab. J. Geosci.* **2015**, *8*, 9877–9886. [[CrossRef](#)]
19. Gansser, A. *Geology of the Himalayas*; John Wiley: New York, NY, USA, 1964; 289p.
20. Rolland, Y.; Pecher, A.; Picard, C. Middle Cretaceous back-arc formation and arc evolution along the Asian margin: The Shyok Suture Zone in northern Ladakh (NW Himalaya). *Tectonophysics* **2000**, *325*, 145–173. [[CrossRef](#)]
21. Hussain, A.; Shah, M.T.; Arif, M.; Agheem, M.H.; Mughal, M.S.; Ullah, S.; Hussain, S.A.; Sadiq, I. Chemical composition of gemstones and characterization of their host pegmatites and country rocks from Chumar Bakhoor, Gilgit–Baltistan, Pakistan: Implications for the source of gem-forming fluids. *Arab. J. Geosci.* **2021**, *14*, 1303. [[CrossRef](#)]
22. Hassan, M. Mineralogy and Geochemistry of the Gemstones and Gemstone-Bearing Pegmatites in Shigar Valley of Skardu, Northern Areas of Pakistan. Ph.D. Thesis, University of Peshawar, Peshawar, Pakistan, 2007; 384p.
23. Agheem, M.H.; Shah, M.T.; Khan, T.; Laghari, A.; Dars, H. Field features and petrography used as indicators for the classification of Shigar valley pegmatites, Gilgit–Baltistan region of Pakistan. *Himal. J. Earth Sci. Univ. Peshawar* **2011**, *44*, 1–7.
24. Lu, P.R.; Yao, W.G.; Zhang, H.D.; Yu, X.L.; Yang, B.; Meng, G.; Tian, H.P. Nd Isotopic Compositions of the Diorites from Typical Deposits in Reko Dig Porphyry Cu–Au–Ore–Concentrated Area, Pakistan and Their Tracer Significances. *Acta Geol. Sin.* **2016**, *90*, 2803–2817.
25. Blauwet, D.; Smith, B.; Smith, C. A guide to the mineral localities of the Northern Areas, Pakistan. *Mineral. Rec.* **1997**, *28*, 183.
26. Seong, Y.B.; Bishop, M.P.; Bush, A.; Clendon, P.; Copland, L.; Finkel, R.C.; Kamp, U.; Owen, L.A.; Shroder, J.F. Landforms and landscape evolution in the Skardu, Shigar and Braldu valleys, central Karakoram. *Geomorphology* **2009**, *103*, 251–267. [[CrossRef](#)]
27. Agheem, M.H.; Shah, M.T.; Khan, T.; Murata, M.; Arif, M.; Dars, H. Shigar valley gemstones, their chemical composition and origin, Skardu, Gilgit–Baltistan, Pakistan. *Arab. J. Geosci.* **2014**, *7*, 3801–3814. [[CrossRef](#)]
28. Oktyabr'skii, R.A.; Korchagin, A.M. 'Siberian Emerald' (History of Discovery and New Data). *Vestn. Dal'nevost. Otd. Ross. Akad. Nauk* **2000**, *4*, 29–36.

29. Naumov, V.B.; Kamenetsky, V.S.; Thomas, R.; Kononkova, N.N.; Ryzhenko, B.N. Inclusions of silicate and sulfate melts in chrome diopside from the Inagli deposit, Yakutia, Russia. *Geochem. Int.* **2008**, *46*, 554–564. [[CrossRef](#)]
30. Naumov, V.B.; Tolstykh, M.L.; Grib, E.N.; Leonov, V.L.; Kononkova, N.N. Chemical composition, volatile components, and trace elements in melts of the Karymskii volcanic center, Kamchatka, and Golovnina volcano, Kunashir Island: Evidence from inclusions in minerals. *Petrology* **2008**, *16*, 1–18. [[CrossRef](#)]
31. Chayka, I.F.; Sobolev, A.V.; Izokh, A.E.; Batanova, V.G.; Batanova, S.P.; Chervyakovskaya, M.V.; Kontonikas-Charos, A.; Kutyr, A.V.; Lobastov, B.M.; Chervyakovskiy, V.S. Fingerprints of Kamafugite-like magmas in Mesozoic lamproites of the Aldan Shield: Evidence from olivine and olivine-hosted inclusions. *Minerals* **2020**, *10*, 337. [[CrossRef](#)]
32. Trunilina, V.A.; Prokopiev, A.V. Ore-Bearing Magmatic Systems with Complex Sn–Au–Ag Mineralization in the North-Eastern Verkhoynsk–Kolyma Orogenic Belt, Russia. *Minerals* **2021**, *11*, 266. [[CrossRef](#)]
33. Patskevich, G.P. The Inagli deposit of jewelry Cr-diopside. In *Gems and Colored Stones [in Russian]*; Nauka: Moscow, Russia, 1980; pp. 146–157.
34. Wang, X.; Hou, T.; Wang, M.; Zhang, C.; Zhang, Z.C.; Pan, R.H.; Marxer, F.; Zhang, H.L. A new clinopyroxene thermobarometer for mafic to intermediate magmatic systems. *Eur. J. Mineral.* **2021**, *33*, 621–637. [[CrossRef](#)]
35. Xu, B.; Hou, Z.Q.; Griffin, W.L.; Lu, Y.J.; Belousova, E.; Xu, J.F.; O'Reilly, S.Y. Recycled volatiles determine fertility of porphyry deposits in collisional settings. *Am. Mineral.* **2021**, *106*, 656–661. [[CrossRef](#)]
36. Xu, B.; Hou, Z.Q.; Griffin, W.L.; Yu, J.X.; Long, T.; Zhao, Y.; Wang, T.; Fu, B.; Belousova, E.; O'Reilly, S.Y. Apatite halogens and Sr–O and zircon Hf–O isotopes: Recycled volatiles in Jurassic porphyry ore systems in southern Tibet. *Chem. Geol.* **2022**, *605*, 120924. [[CrossRef](#)]
37. Xu, B.; Hou, Z.Q.; Griffin, W.L.; Zheng, Y.C.; Wang, T.; Guo, Z.; Hou, J.; Santosh, M.; O'Reilly, S.Y. Cenozoic lithospheric architecture and metallogenesis in Southeastern Tibet. *Earth Sci. Rev.* **2021**, *214*, 103472. [[CrossRef](#)]
38. Omori, K. Analysis of the infrared absorption spectrum of diopside. *Am. Mineral. J. Earth Planet. Mater.* **1971**, *56*, 1607–1616.
39. Schreiber, H.D. On the nature of synthetic blue diopside crystals; the stabilization of tetravalent chromium. *Am. Mineral.* **1977**, *62*, 522–527.
40. Schmetzer, K. Absorptionsspektroskopie und Farbe von V³⁺-haltigen natürlichen Oxiden und Silikaten—ein Beitrag zur Kristallchemie des Vanadiums. *Neues Jahrb. Mineral. Abh.* **1982**, *144*, 73–106.
41. Rossman, G.R. Pyroxene spectroscopy. *Mineral. Soc. Am.* **1980**, *7*, 93–115.
42. Klima, R.L.; Dyar, M.D.; Pieters, C.M. Near-infrared spectra of clinopyroxenes: Effects of calcium content and crystal structure. *Meteorit. Planet. Sci.* **2011**, *46*, 379–395. [[CrossRef](#)]
43. McMillan, P. Structural studies of silicate glasses and melts—applications and limitations of Raman spectroscopy. *Am. Mineral.* **1984**, *69*, 622–644.
44. Mernagh, T.P.; Hoatson, D.M. Raman spectroscopic study of pyroxene structures from the Munni Munni layered intrusion, Western Australia. *J. Raman Spectrosc.* **1997**, *28*, 647–658. [[CrossRef](#)]
45. Huang, E.; Chen, C.H.; Huang, T.; Lin, E.H.; Xu, J.A. Raman spectroscopic characteristics of Mg–Fe–Ca pyroxenes. *Am. Mineral.* **2000**, *85*, 473–479. [[CrossRef](#)]
46. Katerinopoulou, A.; Musso, M.; Amthauer, G. A Raman spectroscopic study of the phase transition in omphacite. *Vib. Spectrosc.* **2008**, *48*, 163–167. [[CrossRef](#)]
47. Buzatu, A.; Buzgar, N. The Raman study of single-chain silicates. *An. Stiintifice Univ. Al. I. Cuza Iași. Sect. 2 Geol.* **2010**, *56*, 107.
48. Chopelas, A. Estimates of mantle relevant Clapeyron slopes in the MgSiO₃ system from high-pressure spectroscopic data. *Am. Mineral.* **1999**, *84*, 233–244. [[CrossRef](#)]
49. Taran, M.N.; Ohashi, H.; Langer, K.; Vishnevskyy, A.A. High-pressure electronic absorption spectroscopy of natural and synthetic Cr³⁺-bearing clinopyroxenes. *Phys. Chem. Miner.* **2011**, *38*, 345–356. [[CrossRef](#)]
50. Morimoto, N.; Fabries, J.; Ferguson, A.K.; Ginzburg, I.V.; Ross, M.; Seifert, F.A.; Zussman, J.; Aoki, K.; Gottardi, G. Nomenclature of pyroxenes. *Am. Mineral.* **1988**, *73*, 1123–1133.
51. Foley, S.F.; Jackson, S.E.; Fryer, B.J.; Greenough, J.D.; Jenner, G.A. Trace element partition coefficients for clinopyroxene and phlogopite in an alkaline lamprophyre from Newfoundland by LAM-ICP-MS. *Geochim. Cosmochim. Acta* **1996**, *60*, 629–638. [[CrossRef](#)]
52. Abedini, A.; Azizi, M.R.; Dill, H.G. The tetrad effect in REE distribution patterns: A quantitative approach to genetic issues of argillic and propylitic alteration zones of epithermal Cu–Pb–Fe deposits related to andesitic magmatism (Khan Kandi District, NW Iran). *J. Geochem. Explor.* **2020**, *212*, 106516. [[CrossRef](#)]
53. Ubide, T.; Kamber, B.S. Volcanic crystals as time capsules of eruption history. *Nat. Commun.* **2018**, *9*, 326. [[CrossRef](#)]
54. Nimis, P. A clinopyroxene geobarometer for basaltic systems based on crystal-structure modeling. *Contrib. Mineral. Petrol.* **1995**, *121*, 115–125. [[CrossRef](#)]
55. Putirka, K.D.; Johnson, M.; Kinzler, R.; Longhi, J.; Walker, D. Thermobarometry of mafic igneous rocks based on clinopyroxene-liquid equilibria, 0–30 kbar. *Contrib. Mineral. Petrol.* **1996**, *123*, 92–108. [[CrossRef](#)]
56. Ravna, K. The garnet–clinopyroxene Fe²⁺–Mg geothermometer: An updated calibration. *J. Metamorph. Geol.* **2000**, *18*, 211–219. [[CrossRef](#)]
57. Nakamura, D. A new formulation of garnet–clinopyroxene geothermometer based on accumulation and statistical analysis of a large experimental data set. *J. Metamorph. Geol.* **2009**, *27*, 495–508. [[CrossRef](#)]
58. Villaseca, C.; Dorado, O.; Orejana, D. Mineral chemistry of megacrysts and associated clinopyroxenite enclaves in the Calatrava volcanic field: Crystallization processes in mantle magma chambers. *Iber. Geol.* **2019**, *45*, 401–426. [[CrossRef](#)]

59. Villaseca, C.; García Serrano, J.; Orejana, D. Pyroxenites and Megacrysts from Alkaline Melts of the Calatrava Volcanic Field (Central Spain): Inferences from Trace Element Geochemistry and Sr–Nd Isotope Composition. *Front. Earth Sci.* **2020**, *8*, 132. [[CrossRef](#)]
60. Frey, F.A.; Green, D.H.; Roy, S.D. Integrated models of basalt petrogenesis: A study of quartz tholeiites to olivine melilitites from South Eastern Australia utilizing geochemical and experimental petrological data. *J. Petrol.* **1978**, *19*, 463–513. [[CrossRef](#)]
61. Conor, C.; Raymond, O.; Baker, T.; Teale, G.; Say, P.; Lowe, G. Alteration and mineralisation in the Moonta–Walleroo copper–gold mining field region, Olympic Domain, South Australia. *Hydrothermal Iron Oxide Copp.-Gold Relat. Depos. Glob. Perspect.* **2010**, *3*, 1–24.
62. Gaspar, M.; Knaack, C.; Meinert, L.D.; Moretti, R. REE in skarn systems: A LA-ICP-MS study of garnets from the Crown Jewel gold deposit. *Geochim. Cosmochim. Acta* **2008**, *72*, 185–205. [[CrossRef](#)]
63. Smith, M.P.; Henderson, P.; Jeffries, T.E.R.; Long, J.; Williams, C.T. The rare earth elements and uranium in garnets from the Beinn an Dubhaich Aureole, Skye, Scotland, UK: Constraints on processes in a dynamic hydrothermal system. *J. Petrol.* **2004**, *45*, 457–484. [[CrossRef](#)]
64. Bea, F. Residence of REE, Y, Th and U in granites and crustal protoliths; implications for the chemistry of crustal melts. *J. Petrol.* **1996**, *37*, 521–552. [[CrossRef](#)]
65. Ismail, R.; Ciobanu, C.L.; Cook, N.J.; Teale, G.S.; Giles, D.; Schmidt Mumm, A.; Wade, B. Rare earths and other trace elements in minerals from skarn assemblages, Hillside iron oxide–copper–gold deposit, Yorke Peninsula, South Australia. *Lithos* **2014**, *184*, 456–477. [[CrossRef](#)]

Disclaimer/Publisher’s Note: The statements, opinions and data contained in all publications are solely those of the individual author(s) and contributor(s) and not of MDPI and/or the editor(s). MDPI and/or the editor(s) disclaim responsibility for any injury to people or property resulting from any ideas, methods, instructions or products referred to in the content.